water

MDPI

Article

Study on the Destabilisation Pattern and Volumetric Water Content Evolution Characteristics of Underground Mining Rock Formations Under Heavy Rainfall Conditions

Xiang Lan [1,2], Yunmin Wang [1], Xiaojun Wang [2] and Jiabo Geng [1,2,*]

[1] Sinosteel Maanshan General Institute of Mining Research Co., Ltd., Maanshan 243000, China; 6720221154@mail.jxust.edu.cn (X.L.)
[2] School of Emergency Management and Safety Engineering, Jiangxi University of Science and Technology, Ganzhou 341000, China
* Correspondence: gengjiabo@jxust.edu.cn

Abstract: In order to study the stability of rock layers and the change in volumetric water content at different stages of mining under an environment of heavy rainfall, a self-developed large-scale open-pit-to-underground-mining similar physical model was used, and the intensity of continuous rainfall was set at 40 mm/h. The results of this study show that fissures accelerated the instability of rock strata, and when spreading to different rock strata, they were prone to form subsidence cracks and produce collapse zones. The volumetric water content is closely related to the stability of the rock formation. An 'arch-shaped collapse zone' was formed in an interval of (0.9~1.8 m), and a convex spreading zone of volumetric water content was formed in an interval of (1.2~1.6 m). The infiltration line shows different diffusion patterns in different mining stages. In the early stage of mining, the volumetric water content infiltration line is roughly parallel to the slope; in the middle stage of mining, the infiltration line diffuses parallel to the two ends of the interface with the slope and diffuses convexly in the middle; in the late stage of mining, the infiltration line shows a pattern of rapid diffusion in the lower area, rapid diffusion in the middle area, and slow diffusion in the middle area. Therefore, in the process of the mining stage, it is necessary to focus on mining area fissure changes and monitor the point water content for sudden changes and other indicators. This study has certain guiding significance for safe production.

Keywords: open-pit-to-underground mining; rock layer destabilisation; volumetric water content; similar tests; numerical simulation

check for updates

Academic Editor: Achim A. Beylich

Received: 18 December 2024
Revised: 5 January 2025
Accepted: 6 January 2025
Published: 7 January 2025

Citation: Lan, X.; Wang, Y.; Wang, X.; Geng, J. Study on the Destabilisation Pattern and Volumetric Water Content Evolution Characteristics of Underground Mining Rock Formations Under Heavy Rainfall Conditions. *Water* **2025**, *17*, 136. https://doi.org/10.3390/w17020136

Copyright: © 2025 by the authors. Licensee MDPI, Basel, Switzerland. This article is an open access article distributed under the terms and conditions of the Creative Commons Attribution (CC BY) license (https://creativecommons.org/licenses/by/4.0/).

1. Introduction

After decades of continuous high-intensity mining, the vast majority of open-pit mines have entered the stage of deep open-pit mining, and most mines are currently transitioning or have already transitioned to underground mining [1,2]. Most mines were stable during the initial phase of mining, but as mining progressed, long-term water infiltration and activities such as excavation can easily lead to disasters such as the collapse of rock layers in working faces and mined-out areas [3–5].

Rainfall is considered an important cause of rock layer collapse [6,7]. Jiang et al. [8] collected 170 cases of rock layer collapse related to rainfall in China and believed that there is a causal relationship between rainfall intensity and rock layer collapse. Haque et al. [9] created a large-scale landslide spatial distribution map for 128 countries and found that

the frequency of landslides in rainbelt areas is significantly higher than in other regions, making them prone to large-scale landslide disasters. Many researchers believe that water has a softening effect on soil strength. When water infiltrates unsaturated soil, the matric suction decreases, the volumetric water content increases, and the stability of the slope decreases [10–14]. Due to the water-retaining properties of soil, some of the water flows along rock layer fractures and faults into deeper underground areas, leading to rock mass damage and crack development, further destabilising the rock layers [15–19].

Underground mining causes disturbances to the underground rock layers, forming an area affected by mining activities [20–22]. Under the influence of mining, fractures develop into interconnected fissures, intense subsidence zones, and localised collapses [23]. Under extreme rainfall conditions, rainwater flows along these channels to the mining face, affecting production and endangering personnel safety [24–26]. Underground mining leads to changes in the volumetric water content around the rock layers. Xu et al. [27] found that the volumetric water content in the mining area can increase by several times to several tens of times based on long-term recorded water level data. Poulsen et al. [28] believe that a permeability increase from the in situ state is predicted to range from approximately eight orders-of-magnitude in the caved zone to one to two orders-of-magnitude in the strata above the fractured zone. Under the influence of mining disturbances, new fractures continuously form in the rock layers, providing pathways for water seepage and transmission [29]. Frash et al. [30] argued that underground shear fractures are the main channels for water seepage, with their permeability being six orders of magnitude higher than that of the adjacent rock matrix. Huang et al. [31] demonstrated through experiments that underground mining creates damage zones, where the lithological characteristics of the rock layers change, thereby affecting the changes in volumetric water content.

Many researchers have focused on the application of saturated–unsaturated seepage theory to volumetric water content changes and slope stability analyses, or on the changes in the volumetric water content and infiltration rate of the mining face as a result of the mining phase. However, the stability of underground rock formation and slope stability are inextricably linked and cannot be separated and studied in isolation.

Therefore, this study took a typical large-scale open-pit-to-underground mining with a model, obtained the necessary parameters through field exploration and drilling sampling, and used a self-developed similar physical model experiment with a rainfall intensity of 40 mm/h. The instability of rock strata in different stages of mining under the condition of heavy rainfall was investigated, and the change in the volumetric water content in rock strata at different stages of mining was explored.

2. Theoretical Analysis

2.1. Basic Principles of MatDEM

MatDEM software (version 3.24) uses an innovative matrix discrete-element calculation method and a three-dimensional contact algorithm. By stacking and cementing particles to construct models, it can effectively simulate rock layer collapse and slope deformation caused by underground ore-body mining. The software allows for the setting of a dispersion coefficient, enabling the particle size to be randomly distributed within a certain range. The constructed particle model has a porous and loose structure, which can effectively simulate unsaturated soil. The linear elastic model is the main feature of the MatDEM software. It uses normal springs and tangential springs to replace the interactions between soil particles, with the normal springs providing tensile strength and the tangential springs providing shear strength (see Figure 1). The tensile strength and shear strength can

be calculated using the following formulas [32]. The following figure presents the normal coefficient and the tangential coefficient.

$$\begin{cases} F_{nMax} = K_n - X_b \\ F_{sMax} = F_{S0} - \mu F_n \end{cases} \quad (1)$$

where F_{nMax} is the tensile strength; X_b is the fracture displacement; F_{sMax} is the shear strength; F_{S0} is the initial shear force; F_n is the normal spring force; and μ is the friction factor.

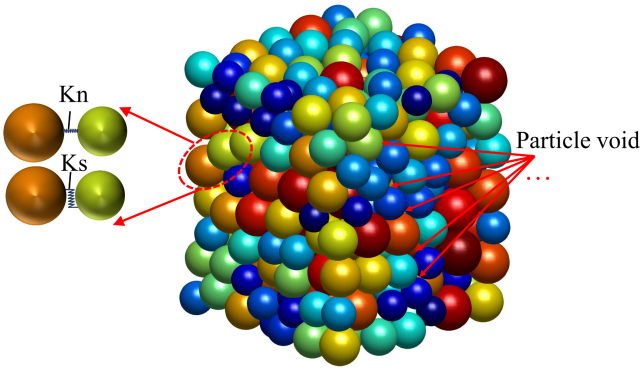


Figure 1. Schematic of particle elastic contact and particle porosity.

To determine whether the particles are undergoing relative motion, it is established that if the contacting particles are in a tensile state, there is no movement; if they are in a compressive state, it is simplified to a sliding model. In MatDEM, the mathematical relationships for the shear force, tangential force, and friction coefficient can be calculated using the following formula:

$$\begin{cases} F_S = F_{s0} + K_s \Delta X_s < -\mu F_n \ (Particle\ slip) \\ F_s = \mu F_n \left(F_{so} + K_s \Delta X_s^3 - \mu F_n \right) \ (Particle\ no\ slip) \end{cases} \quad (2)$$

where F_S is the tangential force of particles; and ΔX_s is the tangential relative displacement increment of particles.

2.2. Boundary Conditions

In saturated–unsaturated seepage calculations, in order to improve the accuracy and reliability of the calculations, the perimeter of the model box should be set as an impermeable boundary, and the corresponding initial and boundary conditions are [10]

$$\begin{cases} H(x,y,t) = H_1(x,y,t) \ (x,y,t) \in \Gamma_1 \\ k_{wx} \frac{\partial H}{\partial x} \cos(\overline{n},x) + k_{wy} \frac{\partial H}{\partial y} \cos(\overline{n},y) = q_n(x,y,t) \ (x,y) \in \Gamma_2 \\ H(x,y,t) = z(x,y,t) \ (x,y) \in \Gamma_3 \\ H(x,y,t_0) = H_0(x,y,t_0) \end{cases} \quad (3)$$

where Γ_1 [0, 1] is the Lknown water head distribution boundary; H_1 is the boundary head; Γ_2 is a known flow boundary; t is the normal flow's unit time boundary; $\cos(\overline{n},x)$ and $\cos(\overline{n},y)$ are the cosine values of the outer boundary surface in the normal direction; Γ_3 is the seepage surface boundary; z is the node coordinate of the seepage surface; and H_0 is the initial condition.

2.3. Slope Stability

In unsaturated soils, the volumetric water content of the soil is closely related to the matrix suction, so when the volumetric water content function is changed, the matrix suction is also changed, which affects the shear strength of unsaturated soils.

$$tan\varphi^b = \left(\frac{\omega - \omega_r}{\omega_s - \omega_r}\right) tan\varphi' \tag{4}$$

Soil shear strength distribution equation:

$$\tau = c' + Ntan\varphi' + \psi tan\varphi^b \tag{5}$$

Here, τ is the shear strength, ω is the volume water content of the soil, ω_s is the saturation volume of the water content of the soil, φ^b is the rate at which the shear strength increases with matric suction, N is the calibration parameter, ω_r is the matrix suction corresponding to the mean volume water content, and c is the effective cohesion of unsaturated soil.

Based on the change in shear strength under the action of volumetric water content, updated Formulas (1) and (2) in the iterative calculation can be used to calculate the stability coefficient of slope under water penetration.

In the case of rainfall infiltration, in considering that the sliding surface of this experiment is located on the wetting line of the overburden slope, the weight of the infiltrated soil is shown in the following equation:

$$G_s(1-n) - \frac{W}{(h-h_s)\Delta S} - \omega_q r_w \tag{6}$$

Here, W is the soil strip weight on the sliding surface, G_s is the soil particle weight, ω_q is the equal rainfall intensity, r_w is the water weight, ΔS is the bottom width of the strip, and h_s is the potential sliding surface height.

$$\begin{aligned} F_s &= \frac{c' + \left\{\left[\omega_q r_w + G_s(1-n)\right](h-h_s)cos\beta\right\} tan\varphi'}{\left[\omega_q r_w + G_s(1-n)\right](h-h_s)sin\beta} \\ &+ \frac{\psi tan\varphi^b}{\left[\omega_q r_w + G(1-n)\right](h-h_s)sin\beta} \end{aligned} \tag{7}$$

3. Model Construction

3.1. Research Background

The Yinshan Lead-Zinc Mine is located in Yincheng Town, Dexing City, Jiangxi Province, and is part of the western section of the Circum-Pacific Metal Mineralization Belt. As shown in Figure 2c, after decades of mining, the mining area has become a large open-pit mine, with the open-pit area being nearly circular. The aquifer in the mining area is mainly composed of structural fracture water, with water seeping and dripping from fault fracture zones. The humid area accounts for 28.6%, while the dripping area accounts for 8.6%.

As shown in Figure 2, after on-site investigation underground, there are fine vein-like joint fractures and seepage around the mine. In some areas, the support above is damaged, and rock has collapsed. The slope of the open-pit mining area is 250 m higher than the bottom of the pit, with an underground mining depth of −200 m, making the total research height of the area 450 m. The geometric similarity constant ratio between the experimental model and the prototype is 1:250.

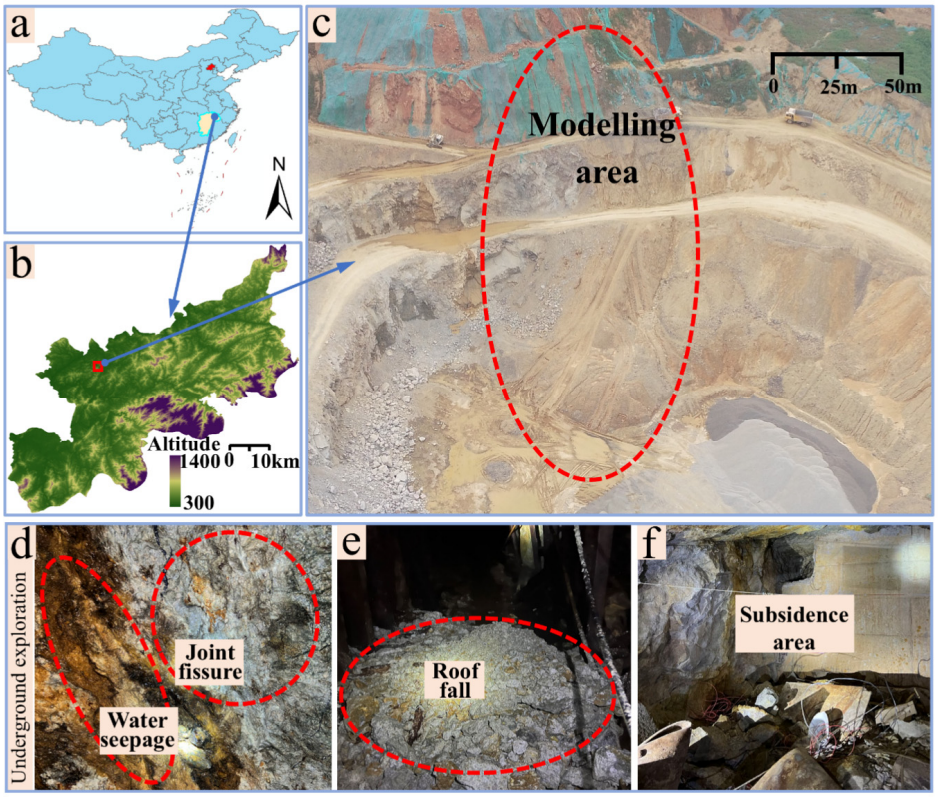


Figure 2. Open-pit and underground exploration. (**a**,**b**) study area location, (**c**) target pit, (**d**) underground roadway fracture, (**e**) roof rock fall, and (**f**) subsidence area.

3.2. Rock Mechanic Parameters

The presence of structural surfaces such as fissures, joints, and faults in the rock formation requires the weakening of the rock's laboratory-measured mechanical parameters (see Table 1). Based on the geological strength index (GSI) and the generalised Hoek-Brown equation [33], the discounted rock mechanical parameters in Table 2 were derived, which provide the basis of mechanical parameters for physically similar experimental proportioning and numerical simulation.

Table 1. Rock mechanic parameters.

Name of Stratum	Compressive Strength/Mpa	Young's Modulus/Gpa	Tensile Strength/Mpa	Poisson's Ratio	Cohesion/Mpa	Angle of Internal Friction/(°)
Loess	4.98	0.77	4.30	0.46	17.80	1.02
Conglomerate	87.92	42.15	12.90	0.22	22.08	44.03
Granite	167.99	27.37	16.80	0.23	26.56	54.90
Sandy phyllite	92.99	43.19	10.20	0.21	20.10	49.20
Dacite porphyry	98.13	51.05	11.08	0.20	18.26	41.80
Phyllite	107.80	66.17	19.22	0.16	33.07	58.03
Ore body	99.87	55.91	17.57	0.14	33.07	58.03

3.3. Physical Model

Figure 3 shows the self-developed rainfall-to-open-pit-to-underground mining rock movement test device. It mainly includes an experimental platform, a rainfall system, and a data monitoring system. The bottom of the experimental platform is made of Q235 steel plate, surrounded by four round steel columns and 90% light-transmitting high-strength tempered glass, measuring 2.4 m in length, 1.6 m in width, and 1.8 m in height. The rainfall

system mainly consists of a water storage tank, a rain gauge, rainfall spray nozzles, and drainage pipes, with the rain gauge measuring within a range of 0 to 120 mm/h. The data monitoring system is composed of 13 volumetric water content sensors connected to a data collector and a computer. The model of the volumetric water content sensor is SMS3, with a probe length of 7 cm, a measurement range of 0 to 100%, and an accuracy of ±3%. As shown in Figure 4, a suction pump is used to extract air from the inflatable gas bag, creating a negative pressure in the chamber to simulate the mining of rock blocks in the corresponding area. The dimensions of the mining chamber are φ150 × 250 mm, and the dimensions of the mining column are φ100 × 180 mm. There are 5 rows of mining chambers, each with 5 gas bags, totalling 25 mining chamber gas bags, and 4 rows of mining columns, each with 5 gas bags, totalling 20 mining column gas bags.

Table 2. Reduced rock mechanic parameters.

Name of Stratum	Compressive Strength/Mpa	Young's Modulus/Gpa	Tensile Strength/Mpa	Poisson's Ratio	Cohesion /Mpa	Angle of Internal Friction/(°)	GSI	α	m_b
Loess	0.33	0.05	0.36	0.46	1.72	1.02	26	0.5075	0.17
Conglomerate	5.89	3.20	1.10	0.22	2.14	44.03	56	0.5037	0.67
Granite	11.23	2.08	1.44	0.23	2.57	54.90	120	0.4998	6.87
Sandy phyllite	6.23	3.28	0.87	0.21	1.95	49.20	67	0.5017	1.64
Dacite porphyry	6.57	3.87	0.95	0.20	1.77	41.80	72	0.5007	1.66
Phyllite	7.22	5.02	1.65	0.16	3.20	58.03	79	0.5006	1.78
Ore body	6.69	4.26	1.51	0.14	2.23	54.23	90	0.5002	1.45

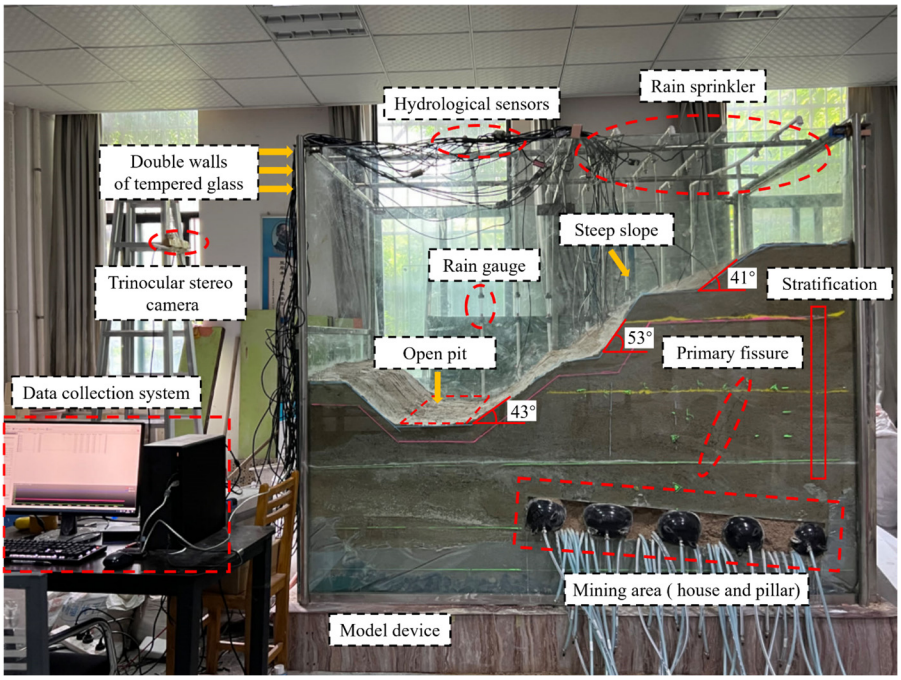


Figure 3. Rock movement test device for rainfall–open-pit-to-underground mining.

The geological survey results indicate that the rock layers in the mining area consist of five parts: the Quaternary loose zone, shallow rock layers, the transition layer of the ore body, ore body layer, and bedrock layer. Based on an engineering report, rock parameters, and multiple preliminary experiments, the material proportions in Table 3 were used to simulate the corresponding rock layers.

Table 3. Rock composition and ratio.

	Name of Stratum	Strata Description	Principal Rock	Rock Quality Index (RQD)	Material Ratio (Coarse Sand, Fine Sand, Lime, Gypsum)
1	Soft region of quaternary system	The thickness is 1~10 m, the rock is loose and weak, and the engineering geological conditions are very poor.	Loess, conglomerate, sandstone	55~62%	10:6:1:2
2	Shallow bed	The average thickness measures approximately 50 m. The rock exhibits significant weathering, extensive fissuring, and poor stability, and is greatly influenced by groundwater activity.	Sandy phyllite, conglomerate	65~75%	6:6:1:2
3	Transition layer	The thickness is greater than 100 m, the rock hardness is slightly lower, and the ore body is indirectly formed; cracks are developed; and the water permeability is good.	Phyllite, sandy phyllite	75~85%	6:4:1:2
4	Ore bed	The surrounding area primarily consists of silicified phyllite with a massive structure, extensive fissure development, and high water permeability.	Phyllite, lead, zinc, silver, ore	80~90%	4:3:1:1
5	Bedrock layer	The rock formation is characterised by its stability, while the surrounding rocks exhibit varying degrees of mineralization.	Dacite porphyry, granite	85~95%	2:2:1:1

Note: The drying time of each rock layer after accumulation is about 48 h.

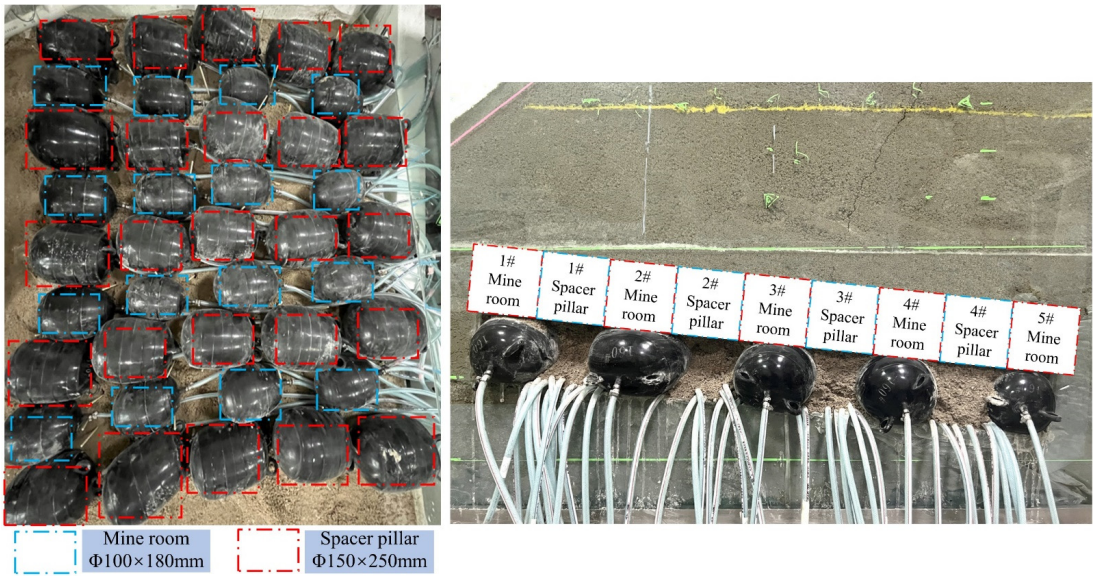


Figure 4. Layout of mine room and pillar.

3.4. Similar Material Selection

In the similarity test simulation, the tolerance weight is the weight link between the model and the prototype. The conversion between mechanical parameters can be reduced when the weight capacity is similar, and the self-gravity field can be simulated more effectively. For the reliability and repeatability of the similarity test, according to Table 3 and the 'Mine Pressure Similarity Simulation Test', we chose common pebbles,

coarse sand, fine sand, lime, gypsum, and water as the main materials, and coloured sand and machine oil as auxiliary materials. After many similar material pre-tests, the materials composed according to the following proportions were selected as the similar materials for this experiment:

(1) Geometric similarity constant: Geometric similarity refers to the ratio of the corresponding spatial dimensions of the model and the prototype. Let the length, width, and height of the model be X_m, Y_m and Z_m, respectively; then, the length, width, and height of the prototype are X_P, Y_P and Z_P respectively, and the geometric similarity constant C_L is

$$C_L = \frac{Y_m}{Y_P} = \frac{X_m}{X_P} = \frac{Z_m}{Z_P} = \frac{1}{250} \tag{8}$$

(2) Time similarity constant: Time similarity is the ratio of the corresponding time dimensions of the model and the prototype. Let the time of the model be T_m; then, the time of the prototype is T_P, and the time similarity constant C_T is

$$C_T = \frac{T_P}{T_m} = \sqrt{C_L} = \frac{63}{1000} \tag{9}$$

(3) Volumetric similarity constant: Let the average volumetric weight of the model formation be R_m; then, the average volumetric weight of the prototype is R_p, and the volumetric similarity constant C_R is

$$C_R = \frac{R_p}{R_m} = \frac{77}{100} \tag{10}$$

where R_m is the prototype bulk weight of 2.2×10^4 N/m^3, and R_p is the modelled bulk weight of 1.7×10^4 N/m^3.

(4) Elastic modulus similarity constant: Let the modulus of elasticity of the model material be E_m, the modulus of elasticity of the prototype material be E_p, and the coefficient of the elastic modulus similarity C_E be

$$C_E = \frac{E_m}{E_p} = C_L \cdot C_R = \frac{77}{25000} \tag{11}$$

(5) Strength-similarity and stress-similarity constants: the strength-similarity and elastic modulus-similarity coefficients are often considered, i.e., strength-similarity and stress-similarity constants C_E = 77/25,000.

(6) The acceleration of gravity is similar to the ratio $\alpha_g = 0.98$ N/kg

3.5. Experimental Scheme

According to existing research data, it is believed that the slope reaches a critical instability stage when the rainfall intensity is 40 mm/h [34]. Therefore, a continuous rainfall intensity of 40 mm/h is set to ensure that the slope surface reaches the maximum saturated volumetric water content. Every 30 min, mining rooms and pillars are excavated, starting from the left to the right (mining rooms 1#, 2#, 3#, 4#, 5#), while maintaining the same direction for the recovery of the pillars (pillars 1#, 2#, 3#, 4#).

3.6. Numerical Simulation Model

Many researchers have used discrete-element software to develop numerical models to study water percolation and transport patterns in soil [32–35]. As shown in Figure 5, a numerical simulation model was built using MatDEM. The model consisted of 800,000 particles with a dispersion coefficient of 0.2 and a particle size distribution of

0.017–0.024 m. A total of 96 h were spent. After several parameter adjustments, the parameters in Tables 4 and 5 were used, and it was considered that the data simulation results could effectively reflect similar experiments. The initial water content was measured with the volumetric water content sensor before experimental mining, and the maximum saturated volumetric water content was the maximum saturated volumetric water content of the experimental mining. In considering the boundary effects, the model boundary conditions were set to be impermeable. Volumetric water content monitoring surfaces and monitoring points were set in the longitudinal plane, section, and level; the naming rules of the monitoring points were by longitudinal plane (L1–L5), section (S1–S5), and level (B1–B5); and the arrangement of monitoring points for the physical experiments is the same as that of the numerical simulation.

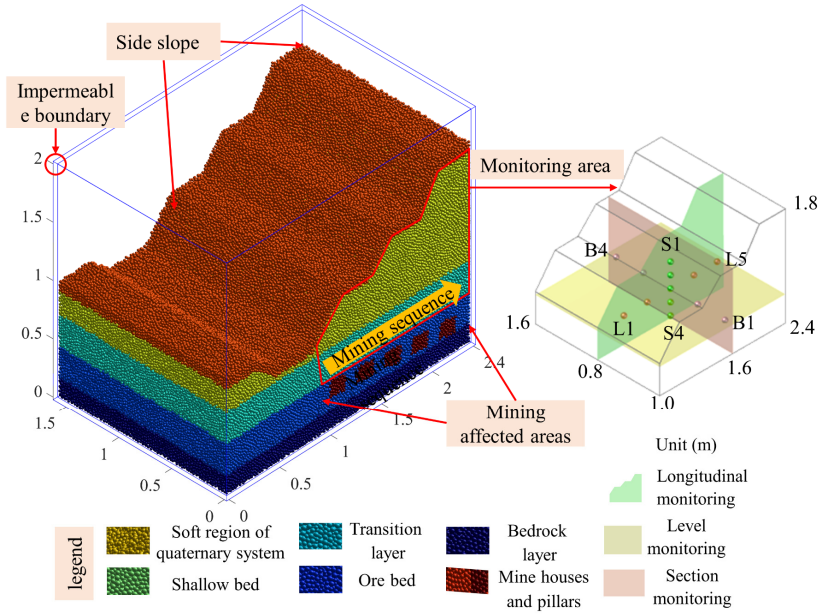


Figure 5. Numerical model and monitoring diagram of open-pit-to-underground mining.

Table 4. Microscopic rock mechanical parameters.

Name of Stratum	Positive Stiffness (K_n/GN·m^{-1})	Tangential Stiffness (K_p/GN·m^{-1})	Fracture Displacement (X_b/m)	Initial Shear Resistance (F_{s0}/GN)	Coefficient of Friction (μ)
Soft region of quaternary system	511.65	102.43	0.0013	2.67	0.0881
Shallow bed	467.53	765.45	0.0024	5.15	0.1426
Transition layer	341.89	117.67	0.0012	3.24	0.0816
Ore bed	491.29	141.67	0.0011	3.78	0.0449
Bedrock layer	619.02	645.45	0.0012	5.93	0.2156

Table 5. Key parameters for numerical simulation.

Length/m	Width/m	Heigh/m	Dispersion Coefficient	Particle Size Distribution/m	Sliding Factor	Number of Cycles/ Times	Standard Equilibrium Constant	Total Number of Particles/ Million	Running Time/h
2.4	1.6	2.4	0.2	0.017–0.024	0.00001	9	0.02	80	96

4. Result Analysis

4.1. Physical Simulation Experiments on the Evolution of Deformation in Rock Formations

Figure 6 shows the changes in rock layers at different mining stages. Figure 6a illustrates the changes in rock layers after the mining of the #1 mining chamber, while Figure 6b depicts the changes in rock layers after the mining of all chambers. It can be observed that during the mining phase, the slopes and rock layers did not exhibit significant deformation or cracks, with only a small amount of rock and soil falling from the roof of the mining chamber. Figure 6c shows the changes in rock layers after the mining of the #1 mining pillar, where the overall stability of the rock layers is maintained, and no significant collapse is observed; however, numerous new cracks have appeared in the overburden of the #1 mining pillar. In Figure 6d, after the mining of the #2 mining pillar, a large-scale collapse of rock layers occurred in the areas of the #1 mining chamber, #2 mining chamber, #1 mining pillar, and #2 mining pillar. This resulted in the formation of an 'arched collapse zone', located in the interval X (0.9~1.4 m), with a vertical projection area of approximately 0.12 m^2. The top of the 'arched collapse zone' produced primary and secondary cracks, which penetrated through the ore body layer and the transition layer of the ore body. Field measurements indicated that the primary crack is parallel to the slope, extending to the boundary between the ore body transition layer and the shallow rock layer, with a length of approximately 0.356 m and a maximum width of about 0.08 m. After the mining of the #4 mining pillar, a large-scale collapse of rock layers occurred, located in the interval X (0.9~1.8 m). The large collapse area can be divided into three parts. The first part is the collapse area of the original No. 2 mining pillar. The second part is the collapse area of the ore body layer and the ore body transition layer, defined by the existing main fissures. The third part is the collapse area of the shallow rock layer, defined by the extension fissures derived from the main fissures. The vertical projection areas of the three collapse zones are approximately 0.12 m^2, 0.34 m^2, and 0.08 m^2, respectively. During this mining phase, the main fissure spreads upward along a direction parallel to the slope, reaching the top area of the shallow rock layer, with a length of about 0.484 m and a maximum width of about 0.023 m. Additionally, as the main fissure extends into the shallow rock layer, significant subsidence cracks appear at the interface of the bottom of the shallow rock layer, causing the ore body transition layer to separate from the shallow rock layer, forming the second collapse area. The length of this subsidence crack is approximately 0.168 m, with a maximum width of about 0.016 m. Changes in the ore house and pillars were as follows: When the ore house was mined, the deformation of the ore house and pillars was not obvious, and no large-scale collapse occurred. When the pillars were being mined, several large-scale nascent fissures and local area-scale collapses appeared, indicating that the later stages of mining greatly undermined the stability of the rock layer.

As mining progresses, primary fractures will give rise to secondary fractures, which exacerbate the propagation of primary fractures. The direction of fracture propagation is parallel to the slope orientation. When fractures extend into different rock layers, they form subsidence cracks, and the combined effect with surrounding fractures causes the two types of rock layers to separate, resulting in a collapse zone. Additionally, the primary fractures penetrate the ore body layer, the transitional layer of the ore body, and the shallow rock layers, allowing external water to flow through numerous primary and secondary fractures. Due to the softening effect of water on the rock mass, this will increase the instability of the rock layers and generate more fractures. Under the interaction of water and fractures, the collapse of rock layers occurs in a 'domino effect', further forming a collapse zone.

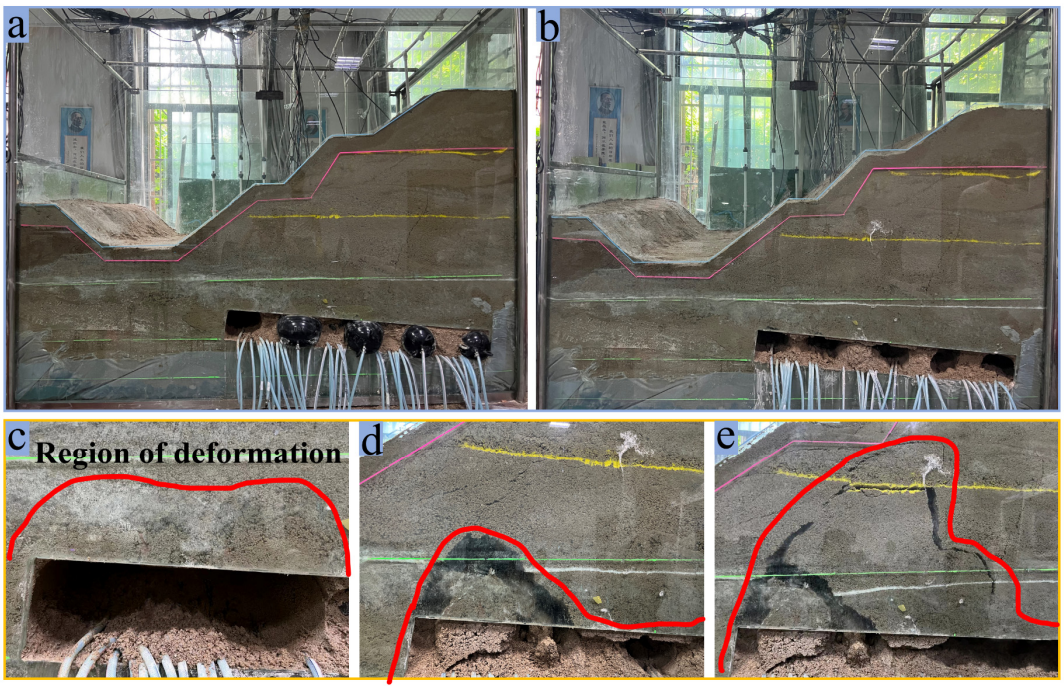


Figure 6. Rock strata change map from open-pit-to-underground mining. (**a**) mining rooms 1#, (**b**) mining all rooms, (**c**) mining pillars 1#, (**d**) mining pillars 2#, and (**e**) mining all pillars.

4.2. Characteristics of Volumetric Water Content Evolution in Physical Simulation Experiments

After 10 days of natural air drying, the volumetric water content of the rock layer was 14% to 16%. Experimental measurements show that the saturated volumetric water content at the slope surface is 60%. Figure 7a presents the changes in volumetric water content at 13 monitoring points, with representative monitoring points L1, S1, and B1 selected for analysis based on their longitudinal, cross-sectional, and layer characteristics. During the mining room extraction phase, the increases in volumetric water content at monitoring points L1, S1, and B1 are 11.4%, 12.4%, and 8.1%, respectively. In the pillar extraction phase, the increases in volumetric water content are 19.6%, 21.6%, and 19.7%, respectively. As mining progresses, the increase in volumetric water content during the mining room extraction phase is less than that during the pillar extraction phase, indicating that the increased rate of volumetric water content in the mining room extraction phase V_1 is less than that in the pillar extraction phase V_2.

The change in volumetric water content is related to the stability of the rock layers. In taking monitoring point L1 as an example, this monitoring point is located above the #1 mining chamber (X = 0.95 m, Y = 0.8 m, Z = 0.65 m). During the mining phase of the chamber, the rock layers were relatively stable, and no new cracks were observed. The volumetric water content slowly increased during this phase, with a growth rate of 1.44×10^{-3}. When the #1 mining pillar was extracted, the rate of increase in volumetric water content accelerated, with a slope of 1.49×10^{-3}. The extraction of the #2 mining pillar resulted in the formation of primary and secondary cracks, leading to a significant increase in volumetric water content, with a slope of 1.56×10^{-3}. During the extraction of the #3 mining pillar, the rock layers remained relatively stable, and the increase in volumetric water content was slightly higher than in the previous phase, with a slope of 1.63×10^{-3}. The extraction of the #4 mining pillar resulted in the formation of three collapse zones and numerous cracks, causing a sudden increase in volumetric water content, with a slope of 1.75×10^{-3}. Monitoring points L1, L2, L3, L4, and L5 are distributed at equal intervals of 0.25 m. As shown in Figure 7c, the more stable the rock layer area, the smaller the change in volumetric water content.

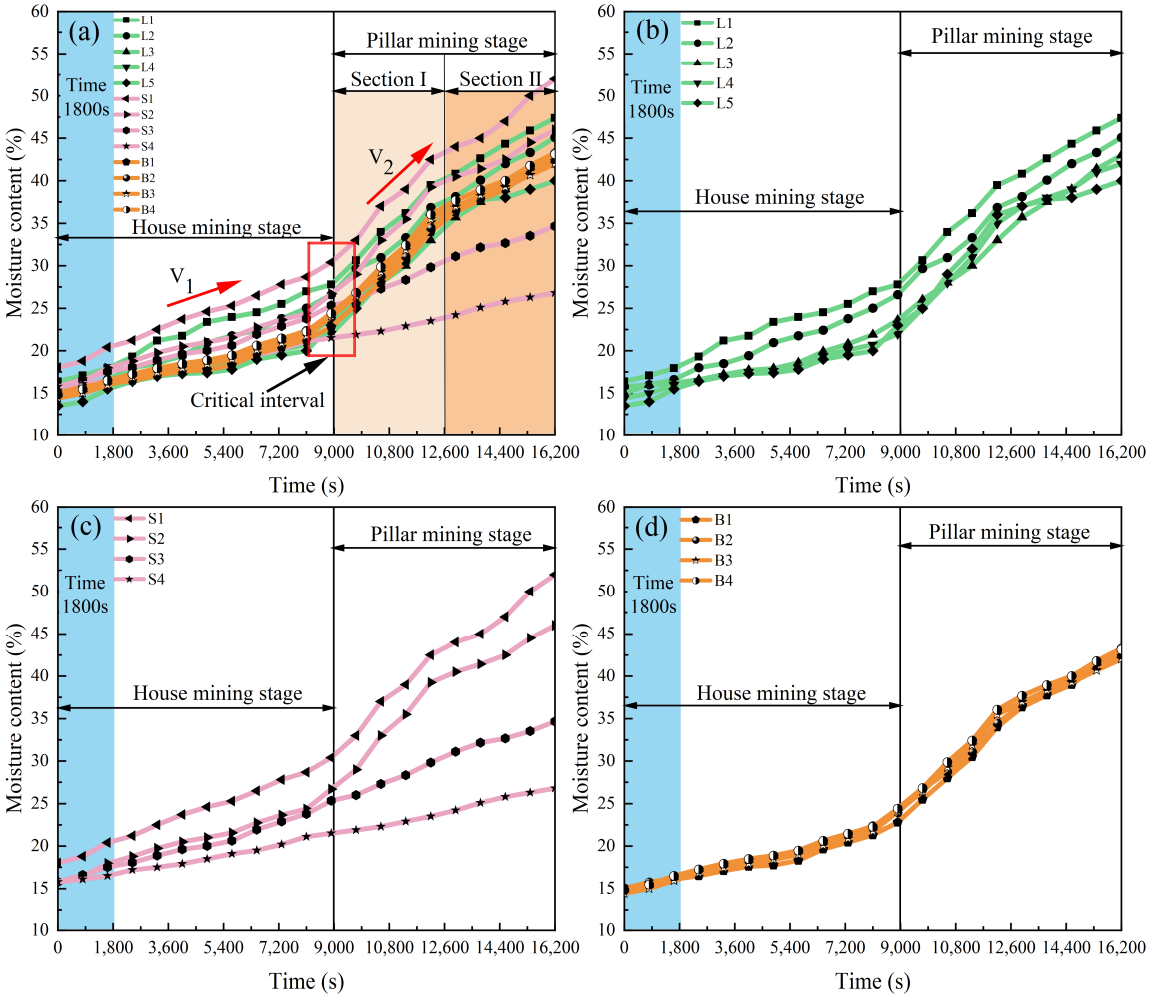


Figure 7. Change curve of volumetric water content at monitoring points. (**a**) Volumetric water content changes at all monitoring points, (**b**) X axis monitoring point volume water content change, (**c**) Y axis monitoring point volume water content change, and (**d**) Z axis monitoring point volume water content change.

4.3. Cloud Map Verification of the Numerical Simulation's Volume Water Content

Figure 8A–J are contour maps of volumetric water content based on similar physical experimental data interpolated using MatLab software (version R2022a). Figure 8a–j are contour maps of volumetric water content generated from numerical simulation experimental data. As shown in Figure 8A,a, after natural air drying, the volumetric water content gradually increases from the outer layer to the deeper layers. In Figure 8B–F,b–f, during the mining phase of the mine, the wetting front (the contour line where the volumetric water content is 0.15) was roughly parallel to the slope interface. The average vertical distances from the slope are 0.134 m, 0.136 m, 0.151 m, 0.165 m, and 0.204 m, with wetting areas of 0.182 m^2, 0.188 m^2, 0.199 m^2, 0.218 m^2, and 0.243 m^2, respectively. During the mining phases from the #1 mine to #5 mine, the diffusion rate of the wetting front is relatively slow. This is mainly because the rock layers are relatively stable, the slope has not undergone significant deformation, and the mined rock layers have not developed noticeable fractures or collapses. In Figure 8G,g, after the mining of the #1 pillar is completed, the wetting front undergoes local deformation, bulging toward the deep rock layer in interval X (1.2~1.6 m). This reflects that the volume water content diffusion rate in the central region is higher than that at the top and bottom. During this mining process, the wetting front diffuses parallel to the slope interface, transforming into a state where the wetting front diffuses parallel to both ends of the slope interface, with a bulging shape in the middle. The average

vertical distance from the wetting front to the slope is 0.235 m, and the wetting area is 0.268 m^2. In Figure 8H,h, after the mining of the #2 pillar is completed, the average vertical distance from the wetting front to the slope is 0.293 m, and the wetting area is 0.284 m^2. It can be observed that the bulging area of the wetting front has further expanded and developed toward the deep rock layer. This is mainly due to a large-scale rock collapse that occurred during this stage, forming an 'arched collapse zone', where the main fracture area overlaps with the bulging area of the wetting front. Figure 8I,i, after the end of mining of the #3 pillars, the average distance of the infiltration line toward the slope is 0.353 m, and the infiltration area is 0.328 m^2. The volumetric water content at the bottom of the slope changed significantly and increased along the X axis toward the deeper part of the slope, which is mainly due to the spreading of secondary fissures derived from the main fissures to the foot of the slope area, which is conducive to the transmission of water. Figure 8J,j, after the end of the mining of the #4 pillar, the average distance of the infiltration line drooping to the slope is 0.392 m, and the infiltration area is 0.372 m^2. The change in volumetric water content at this stage is the largest in the whole mining process. It is mainly because the large-scale rock collapse occurred in this stage, which produced numerous rock fissures and obvious subsidence cracks, and these conditions greatly facilitated water seepage and transmission.

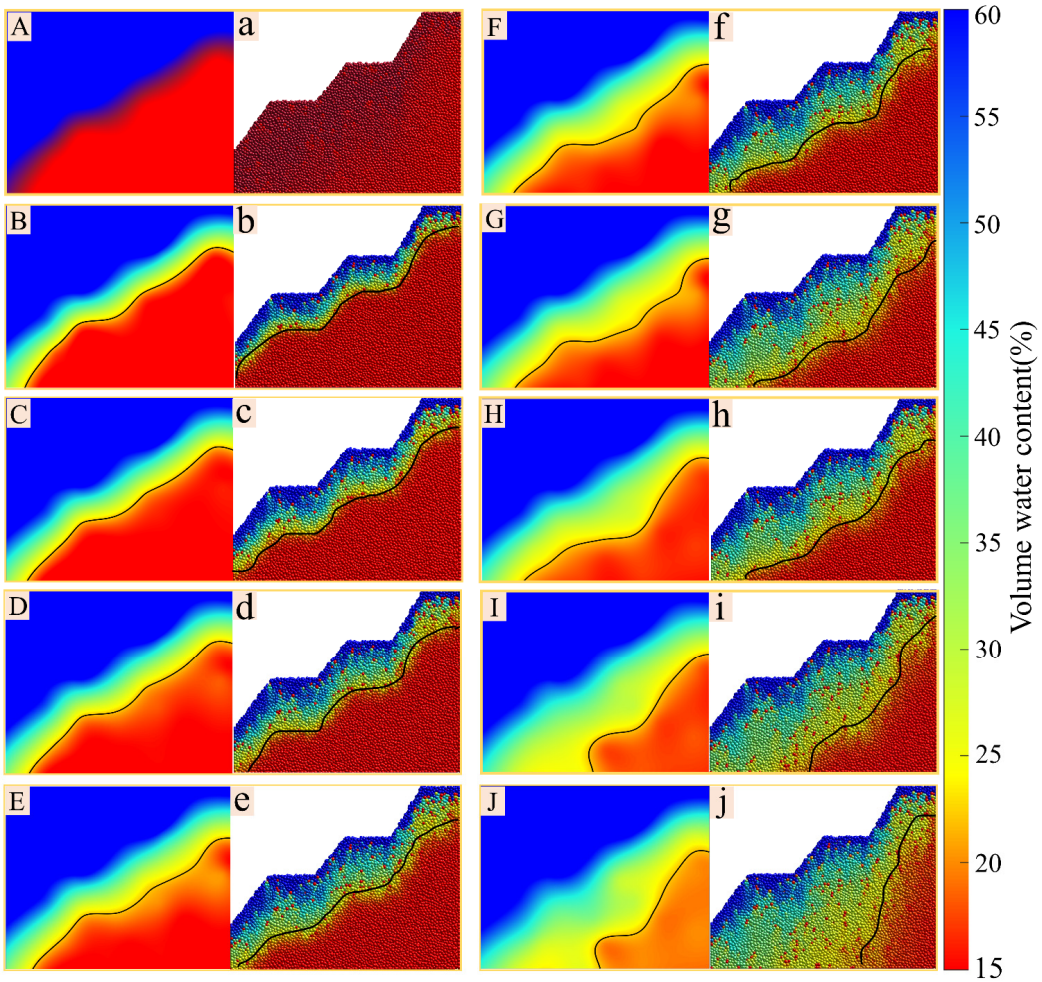


Figure 8. (**A**–**J**) experimental data interpolated vertical volume water content cloud map, and (**a**–**j**) vertical volume water content cloud image of numerical simulation experiment.

As can be seen from Figure 9, with the advancement of mining, the rock layer gradually becomes unstable, the slope stability coefficient gradually decreases, and the av-

erage distance of infiltration line toward the slope, infiltration area, and deformation volume of overlying rock gradually increase. The slope stability coefficient decreased from 1.82 to 1.02, the deformation volume of overlying rock reached 2.05 m^3, the average distance of from the infiltration line to the slope was 0.392 m, and the infiltration area reached 0.32 m^2. In general, the change in volumetric water content is closely related to the stability of the rock formation, and the change in volumetric water content can be summarised in three stages: a slow growth stage, convex diffusion stage, and rapid diffusion stage. And the change in the rock formation deformation can be summarised in three stages: a relatively stable stage, fissure development stage, and collapse zone development stage.

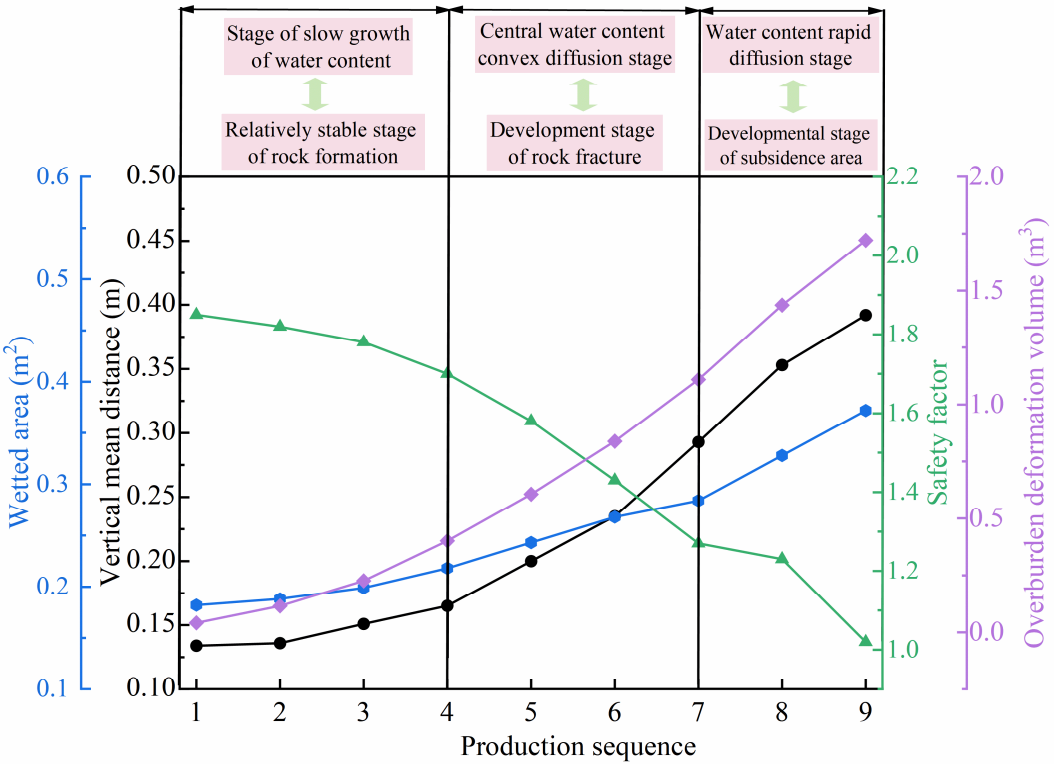


Figure 9. Average distance of vertical slope, infiltrated area, slope stability coefficient, and overburden deformation volume change curve.

Figure 10 shows the cloud map of the volumetric water content distribution in the section, with the same command rule as above. In Figure 10B–F,b–f, the infiltration line remains horizontal with the step and spreads to the depth, and the middle area spreads slightly faster. In these five mining stages, the average distance of the infiltration line to the slope is 0.102 m, 0.107 m, 0.119 m, 0.125 m, and 0.154 m, and the infiltration area is 0.139 m, 0.146 m, 0.155 m, 0.173 m, and 0.223 m, respectively. As shown in Figure 10G–J,g–j, the infiltration line diffusion speed is gradually accelerated, and the intermediate region is slightly faster. The infiltration line develops convexly toward the deep part of the rock formation, and the convex interval is located in the collapsed area formed by subsequent mining. The average distance of the infiltration line to the slope is 0.182 m, 0.225 m, 0.272 m, and 0.312 m, and the infiltration area is 0.245 m, 0.308 m, 0.373 m, and 0.431 m. The average distance of the infiltration line to the slope is 0.245 m, 0.308 m, 0.373 m, and 0.431 m.

Figure 11 shows the cloud map of the volumetric water content distribution at the level. As shown in Figure 11B,b,C,c, the volumetric water content changes slowly and does not reach the maximum saturated volumetric water content due to the fact that the level is 0.3 m away from the slope, not in direct contact with the rainfall, and that the

rock layer remains in a relatively stable stage at this stage. As in Figure 11D–F,d–f, the water diffusion speed is accelerated, the volumetric water content increases and reaches the saturated volumetric water content, and the infiltration line spreads to the deeper part of the rock layer parallel to the slope. In Figure 11G–J,g–j, the moisture transfer rate gradually increases, and the infiltration line in the central region develops convexly toward the deep part of the rock formation, similarly to the distribution of the cross-section.

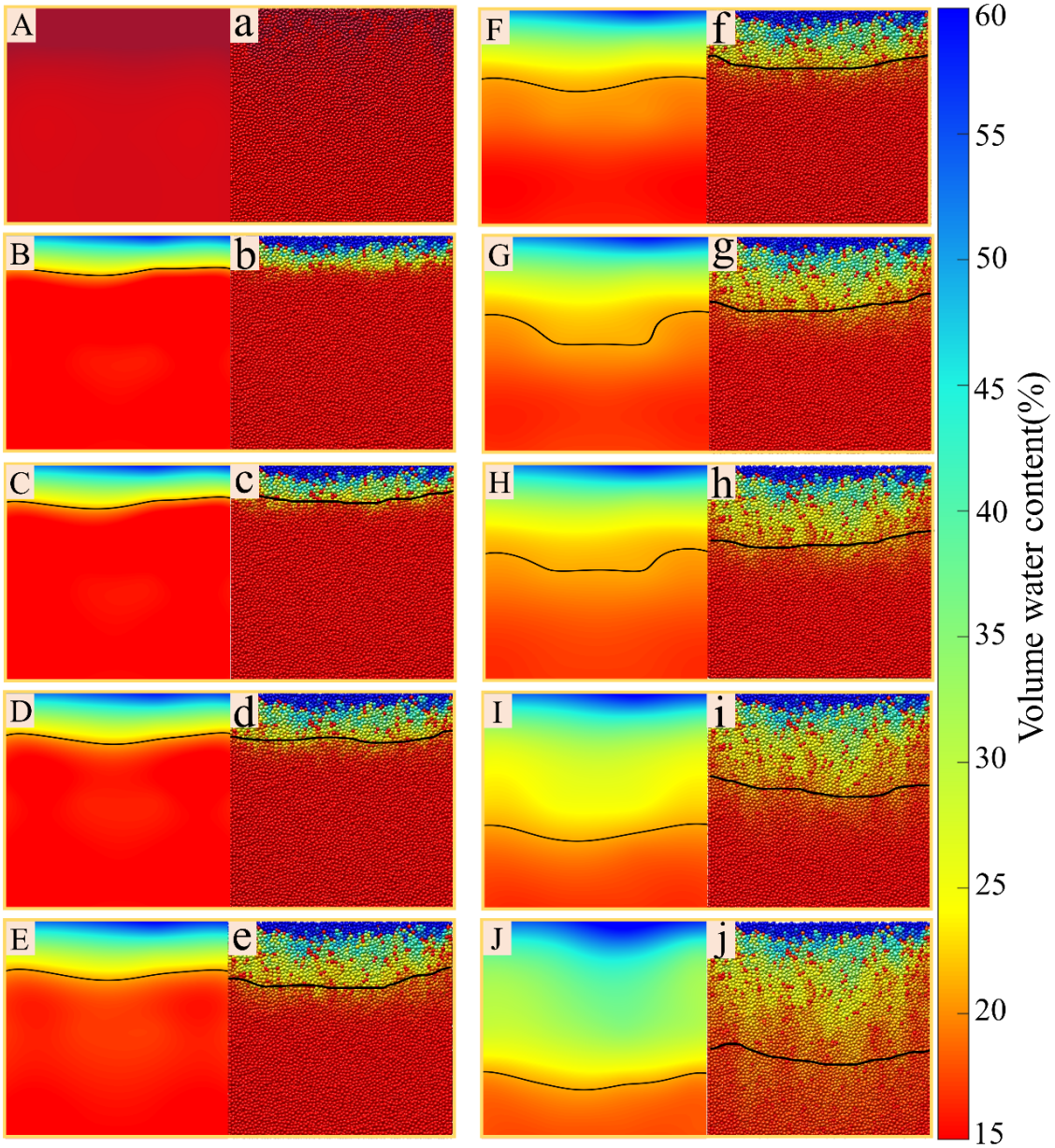


Figure 10. (**A**–**J**) experimental data interpolated section volume water content cloud map, and (**a**–**j**) numerical simulation experiment section volume moisture cloud map.

In general, there is a strong correlation among the zone of sudden changes in volumetric water content and the main fissure area and the collapse area. This is instructive in preventing the formation of cave-in disasters. As mining advances, the rock formation as a whole remains stable. However, the deformation of the rock formation in localised areas, which is often difficult to observe from the surface, can be monitored through changes in volumetric water content to monitor deformation and the creation of unstable areas. In addition, water seepage and transport during open-pit-to-underground mining can be divided into three stages. In the early stage of underground mining, the volumetric water

content infiltration line is roughly parallel to the slope and advances to the deeper part of the rock formation at a slow rate. In the middle stage of downhole mining, the volumetric water content infiltration line spreads parallel to the interface between the volumetric water content infiltration line and the side slope at both ends, spreads convexly in the middle, and pushes forward to the deeper part of the rock formation at a faster speed. In the late stage of underground mining, the volumetric water content infiltration line shows the pattern of fast diffusion in the lower area, faster diffusion in the middle area, and slower diffusion in the middle area, and it no longer maintains a parallel relationship with the slope and advances to the depth.

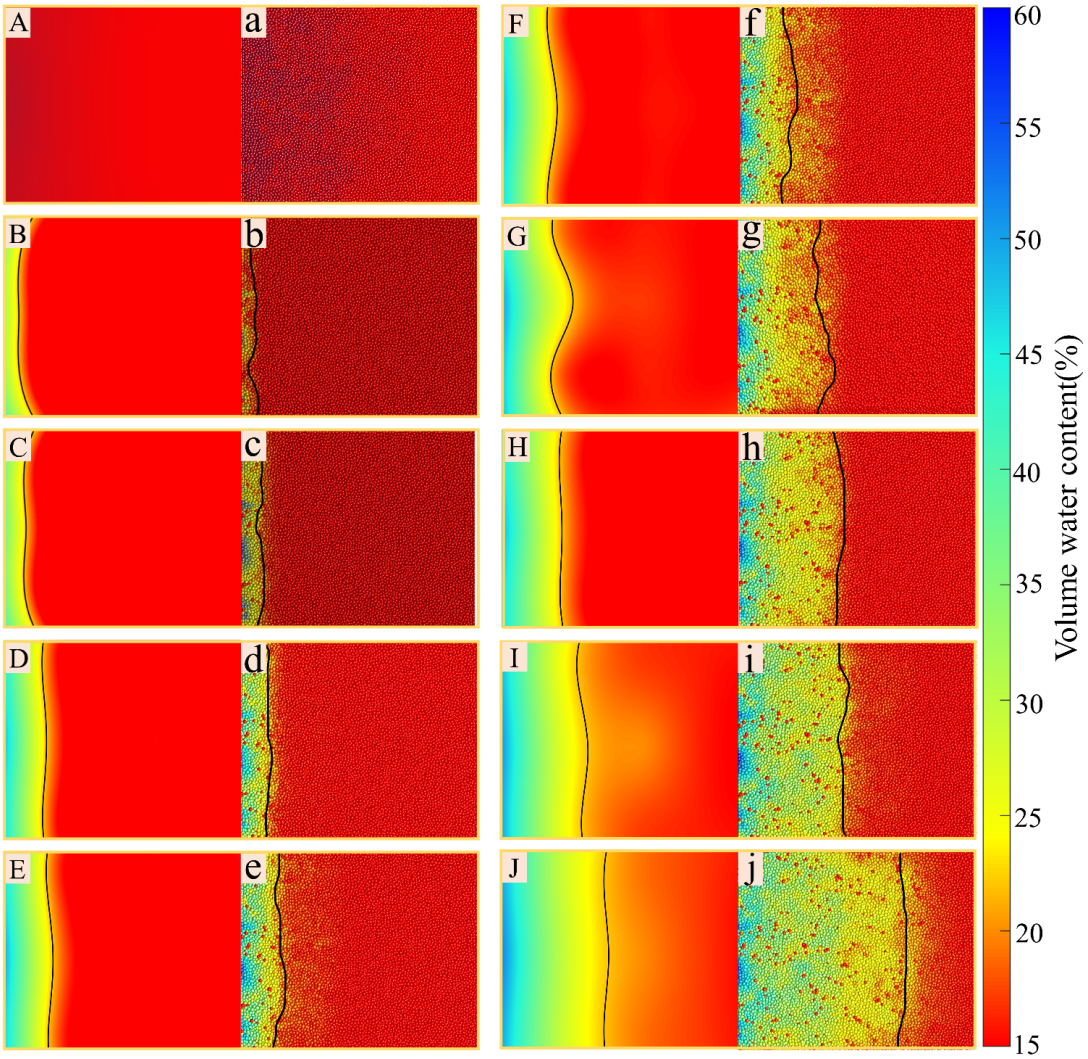


Figure 11. (**A**–**J**) experimental data interpolated layer volume water content cloud map, and (**a**–**j**) numerical simulation experiment layer volume water content cloud map.

5. Conclusions

In order to investigate the stability of rock layers and the change rule of volumetric water content in different mining stages under an environment of strong rainfall, this study took a typical open-pit-to-underground mining mine as the research object, established similar physical model experiments, and obtained modelled longitudinal plane, level, and section volumetric water content change cloud maps by interpolating the experimental data, as verified using the volumetric water content data obtained with the numerical simulation model for each. The main conclusions are as follows:

(1) Fissures accelerate the instability of the rock layer. The direction of fissure spreading is parallel to the slope direction. When spreading to different rock layers, sinking cracks may be formed, which, together with the surrounding fissures, will detach the rock layer and produce a collapse zone. The water spreads to the deeper rock layer through many fissures. Under the weakening interaction of fissures and water, the rock layer collapses in a 'domino' effect, further forming an unstable area. In this experiment, the maximum length of the fissure is 0.484 m, the length of the subsidence crack is about 0.168 m, and the maximum vertical longitudinal projection area of the collapse zone is about 0.54 m^2.

(2) Volumetric water content is closely related to the stability of the rock formation. As mining advances, an 'arch-shaped collapse zone' is formed in an interval X (0.9~1.8 m), while a convex diffusion zone of volumetric water content is formed in an interval X (1.2~1.6 m). The stabler the rock layer, the smaller the change in volumetric water content. Therefore, the change in volumetric water content in the mining stage of the ore house is smaller than that in the mining stage of the pillar. In addition, in taking monitoring point L1 (X = 0.95 m, Y = 0.8 m, Z = 0.65 m) as an example, the volumetric water content grows slowly when the rock formation is stable, with a growth slope of 1.44×10^{-3}, and the volumetric water content grows abruptly after the rock formation collapses, with a growth slope of 1.75×10^{-3}.

(3) With the advancement of mining, the rock layer is gradually unstable, the slope stability coefficient gradually decreases, and the average distance of the infiltration line toward the slope, infiltration area, and deformation volume of overlying rock gradually increase. The slope stability coefficient decreased from 1.82 to 1.02, the deformation volume of overlying rock reached 2.05 m^3, the average distance of the infiltration line to the slope was 0.392 m, and the infiltration area reached 0.32 m^2.

(4) At the early stage of mining, the volumetric water content infiltration line is roughly parallel to the slope and spreads slowly to the deep part of the rock layer; at the middle stage of mining, the volumetric water content infiltration line spreads parallel to the two ends of the interface with the slope, and the middle part of the interface is convex and spreads to the deep part of the rock layer at a relatively high speed; at the late stage of mining, the volumetric water content infiltration line shows the pattern of fast diffusion in the lower part of the area, faster diffusion in the middle area, and slower diffusion in the central part of the area.

Author Contributions: X.L.: data curation, formal analysis, writing—original draft, and writing—review and editing. Y.W.: methodology and writing—review and editing. X.W.: project administration, supervision, validation, and writing—review and editing. J.G.: data curation, formal analysis, writing—original draft, and writing—review and editing. All authors have read and agreed to the published version of the manuscript.

Funding: This work was funded by the National Natural Science Foundation of China (52364013), China Postdoctoral Science Foundation Funded Project (2022M722924), and Natural Science Foundation of Jiangxi Province (20232BAB214035).

Data Availability Statement: The original contributions presented in this study are included in the article. Further inquiries can be directed to the corresponding author.

Conflicts of Interest: Xiang Lan, Yunmin Wang and Jiabo Geng were employed by Sinosteel Maanshan General Institute of Mining Research Co., Ltd. The authors declare that they do not have any commercial or associative interest that represents a conflict of interest in connection with the work submitted.

References

1. Li, X.; Wang, Y.; Hu, Y.; Zhou, C.; Zhang, H. Numerical Investigation on Stratum and Surface Deformation in Underground Phosphorite Mining under Different Mining Methods. *Front. Earth Sci.* **2022**, *10*, 831856. [CrossRef]
2. Li, X.; Yang, S.; Wang, Y.; Nie, W.; Liu, Z. Macro-Micro Response Characteristics of Surrounding Rock and Overlying Strata Towards the Transition from Open-Pit to Underground Mining. *Geofluids* **2021**, *2021*, 5582218. [CrossRef]
3. Mu, C.; Yu, X.; Zhao, B.; Zhang, D.; Mao, X.; Zhu, J. The Formation Mechanism of Surface Landslide Disasters in the Mining Area under Different Slope Angles. *Adv. Civ. Eng.* **2021**, *2021*, 6697790. [CrossRef]
4. Solorzano, J.; Morante-Carballo, F.; Montalván-Burbano, N.; Briones-Bitar, J.; Carrión-Mero, P. A Systematic Review of the Relationship between Geotechnics and Disasters. *Sustainability* **2022**, *14*, 12835. [CrossRef]
5. Chung, C.; Li, Z.-Y. Rapid Landslide Risk Zoning toward Multi-Slope Units of the Neikuihui Tribe for Preliminary Disaster Management. *Nat. Hazards Earth Syst. Sci.* **2022**, *22*, 1777–1794. [CrossRef]
6. Wang, J.; Xiao, L.; Zhang, J.; Zhu, Y. Deformation Characteristics and Failure Mechanisms of a Rainfall-Induced Complex Landslide in Wanzhou County, Three Gorges Reservoir, China. *Landslides* **2020**, *17*, 419–431. [CrossRef]
7. Sun, S.-W.; Liu, L.; Hu, J.-B.; Ding, H. Failure Characteristics and Mechanism of a Rain-Triggered Landslide in the Northern Longwall of Fushun West Open Pit, China. *Landslides* **2022**, *19*, 2439–2458. [CrossRef]
8. Jiang, W.; Tan, Y. Heavy Rainfall-Related Excavation Failures in China During 1994 to 2018: An Overview. *Eng. Fail. Anal.* **2021**, *129*, 105695. [CrossRef]
9. Haque, U.; Da Silva, P.F.; Devoli, G.; Pilz, J.; Zhao, B.; Khaloua, A.; Wilopo, W.; Andersen, P.; Lu, P.; Lee, J. The Human Cost of Global Warming: Deadly Landslides and Their Triggers (1995–2014). *Sci. Total Environ.* **2019**, *682*, 673–684. [CrossRef]
10. Tan, Y.; Cao, J.-J.; Xiang, W.-X.; Xu, W.-Z.; Tian, J.-W.; Gou, Y. Slope Stability Analysis of Saturated–Unsaturated Based on the Geo-Studio: A Case Study of Xinchang Slope in Lanping County, Yunnan Province, China. *Environ. Earth Sci.* **2023**, *82*, 322. [CrossRef]
11. Pham, T.A.; Sutman, M.; Medero, G.M. Validation, Reliability, and Performance of Shear Strength Models for Unsaturated Soils. *Geotech. Geol. Eng.* **2023**, *41*, 4271–4309. [CrossRef]
12. Guo, L.; Chen, G.; Gong, S.; Sun, H.; Chantat, K. Analysis of Rainfall-Induced Landslide Using the Extended Dda by Incorporating Matric Suction. *Comput. Geotech.* **2021**, *135*, 104145. [CrossRef]
13. Xiao, Y.; Liu, S.; Wu, H.; Shi, J.; Liu, H. Strengths and Infinite Slope Stability of Unsaturated Soils. *Int. J. Geomech.* **2023**, *23*, 04023237. [CrossRef]
14. Sattler, K.; Elwood, D.; Hendry, M.T.; Huntley, D.; Holmes, J.; Wilkinson, P.B.; Chambers, J.; Donohue, S.; Meldrum, P.I.; Macciotta, R.; et al. Quantifying the Contribution of Matric Suction on Changes in Stability and Displacement Rate of a Translational Landslide in Glaciolacustrine Clay. *Landslides* **2021**, *18*, 1675–1689. [CrossRef]
15. Chen, J.; Zhao, J.; Zhang, S.; Zhang, Y.; Yang, F.; Li, M. An Experimental and Analytical Research on the Evolution of Mining Cracks in Deep Floor Rock Mass. *Pure Appl. Geophys.* **2020**, *177*, 5325–5348. [CrossRef]
16. Li, C.; Zuo, J.; Xing, S.; Du, W.; Chuai, X. Failure Behavior and Dynamic Monitoring of Floor Crack Structures under High Confined Water Pressure in Deep Coal Mining: A Case Study of Hebei, China. *Eng. Fail. Anal.* **2022**, *139*, 106460. [CrossRef]
17. Liu, G.; Ran, G.; Li, Z.; Duan, S.; Su, G.; Yan, C.; Dong, K. An Insight into the Effect of Primary Hidden Microfissures on Mechanical Behaviors and Failure Characteristics of Brittle Basalt. *Theor. Appl. Fract. Mech.* **2023**, *128*, 104138. [CrossRef]
18. Chen, Z.; Ma, C.; Li, T.; He, C. Experimental Investigation of the Failure Mechanism of Deep Granite under High Seepage Water Pressure and Strong Unloading Effect. *Acta Geotech.* **2022**, *17*, 5009–5030. [CrossRef]
19. Kou, M.-M.; Liu, X.-R.; Wang, Z.-Q.; Tang, S.-D. Laboratory Investigations on Failure, Energy and Permeability Evolution of Fissured Rock-Like Materials under Seepage Pressures. *Eng. Fract. Mech.* **2021**, *247*, 107694. [CrossRef]
20. Shu, J.; Jiang, L.; Kong, P.; Wang, P.; Zhang, P. Numerical Modeling Approach on Mining-Induced Strata Structural Behavior by Considering the Fracture-Weakening Effect on Rock Mass. *Appl. Sci.* **2019**, *9*, 1832. [CrossRef]
21. Bai, C.; Yun, M.X.; Wang, J.M. Hazards of Environmental Disruption in Mine Goafs and Stability Evaluation in Gaofeng Mining Area. *Nat. Environ. Pollut. Technol.* **2020**, *19*, 949–956. [CrossRef]
22. Xia, K.; Chen, C.; Liu, X.; Zheng, X.; Zhou, Y.; Song, X.; Yuan, J. Ground Collapse and Caving Mechanisms in Strata Overlying Sublevel Caving Mines: A Case Study. *Bull. Eng. Geol. Environ.* **2023**, *83*, 21. [CrossRef]
23. Li, X.; Li, Q.; Hu, Y.; Teng, L.; Yang, S. Evolution Characteristics of Mining Fissures in Overlying Strata of Stope after Converting from Open-Pit to Underground. *Arab. J. Geosci.* **2021**, *14*, 2795. [CrossRef]
24. Moore, J.P.; Walsh, J.J. Quantitative Analysis of Cenozoic Faults and Fractures and Their Impact on Groundwater Flow in the Bedrock Aquifers of Ireland. *Hydrogeol. J.* **2021**, *29*, 2613–2632. [CrossRef]
25. Zhou, C.-B.; Chen, Y.-F.; Hu, R.; Yang, Z. Groundwater Flow through Fractured Rocks and Seepage Control in Geotechnical Engineering: Theories and Practices. *J. Rock Mech. Geotech. Eng.* **2023**, *15*, 1–36. [CrossRef]
26. Sheldon, H.A.; Crombez, V.; Poulet, T.; Kelka, U.; Kunzmann, M.; Kerrison, E. Realistic Permeability Distributions in Faults and Sediments: The Key to Predicting Fluid Flow in Sedimentary Basins. *Basin Res.* **2023**, *35*, 2118–2139. [CrossRef]

27. Xu, Q.; Wang, G.; Liang, X.; Qu, S.; Shi, Z.; Wang, X. Determination of Mining-Induced Changes in Hydrogeological Parameters of Overburden Aquifer in a Coalfield, Northwest China: Approaches Using the Water Level Response to Earth Tides. *Geofluids* **2021**, *2021*, 5516997. [CrossRef]
28. Poulsen, B.A.; Adhikary, D.; Guo, H. Simulating Mining-Induced Strata Permeability Changes. *Eng. Geol.* **2018**, *237*, 208–216. [CrossRef]
29. Yang, T.H.; Liu, J.; Zhu, W.C.; Elsworth, D.; Tham, L.G.; Tang, C.A. A Coupled Flow-Stress-Damage Model for Groundwater Outbursts from an Underlying Aquifer into Mining Excavations. *Int. J. Rock Mech. Min. Sci.* **2007**, *44*, 87–97. [CrossRef]
30. Frash, L.P.; Carey, J.W.; Ickes, T.; Viswanathan, H.S. Caprock Integrity Susceptibility to Permeable Fracture Creation. *Int. J. Greenh. Gas Control* **2017**, *64*, 60–72. [CrossRef]
31. Huang, Z.; Jiang, Z.; Zhu, S.; Wu, X.; Yang, L.; Guan, Y. Influence of Structure and Water Pressure on the Hydraulic Conductivity of the Rock Mass around Underground Excavations. *Eng. Geol.* **2016**, *202*, 74–84. [CrossRef]
32. Geng, J.; Wang, Z.; Lan, X.; Li, X.; Zhang, D. Numerical Simulation and Safety Distance Analysis of Slope Instability of Ionic Rare Earth Tailings in Different Rainy Seasons. *Geomat. Nat. Hazards Risk* **2023**, *14*, 2277127. [CrossRef]
33. Xia, K.; Chen, C.; Wang, T.; Zheng, Y.; Wang, Y. Estimating the Geological Strength Index and Disturbance Factor in the Hoek–Brown Criterion Using the Acoustic Wave Velocity in the Rock Mass. *Eng. Geol.* **2022**, *306*, 106745. [CrossRef]
34. Li, X.; Li, Q.; Wang, Y.; Liu, W.; Hou, D.; Zheng, W.; Zhang, X. Experimental Study on Instability Mechanism and Critical Intensity of Rainfall of High-Steep Rock Slopes under Unsaturated Conditions. *Int. J. Min. Sci. Technol.* **2023**, *33*, 1243–1260. [CrossRef]
35. Gu, X.; Nie, W.; Li, Q.; Geng, J.; Zhou, T.; Yuan, C. Discrete Element Simulation of the Road Slope Considering Rainfall Infiltration. *Water* **2022**, *14*, 3663. [CrossRef]

Disclaimer/Publisher's Note: The statements, opinions and data contained in all publications are solely those of the individual author(s) and contributor(s) and not of MDPI and/or the editor(s). MDPI and/or the editor(s) disclaim responsibility for any injury to people or property resulting from any ideas, methods, instructions or products referred to in the content.